Chemical
Science

ROYAL SOCIETY
OF CHEMISTRY

EDGE ARTICLE

View Article Online
View Journal | View Issue

Check for updates

Cite this: *Chem. Sci.*, 2025, **16**, 19849

All publication charges for this article have been paid for by the Royal Society of Chemistry

Received 25th June 2025
Accepted 17th September 2025

DOI: 10.1039/d5sc04675k

rsc.li/chemical-science

Dual-catalytic architectures accommodated by titanium-oxo clusters boosting visible-light-driven C–N cross-coupling *via* intramolecular electron transfer

Shiyu Wang,[a] Jianfeng Jia,[a] Yongqi Wang,[a] Qiang Gao *[b] and Gang Ye *[a]

Developing dual-catalytic architectures integrating photoactive and transition metal sites holds significant potential for light-driven cross-coupling reactions. This study presents a novel strategy to create synergistic dual-catalytic architectures based on surface engineering of Ti_6-oxo clusters for efficient photocatalytic formation of C–N bonds. Ti_6-oxo clusters are precisely decorated with bipyridine ligands through competitive coordination, followed by the anchoring of iridium photo-sensitizers and nickel catalytic centers to the electron-rich nitrogen sites. The obtained Ni–Ir/Ti_6-Bpca exhibits significantly enhanced charge transfer efficiency *via* an intramolecular electron transfer mechanism. This integrated design not only boosted catalytic activity across diverse substrates but also suppressed metal site leaching and nickel black formation through the coordination protection effect. The Ni–Ir/Ti_6-Bpca system achieved remarkable functional group tolerance with reduced catalyst loading under visible light irradiation (blue light, $\lambda_{max} = 430$ nm). By demonstrating enhanced electron transfer kinetics and operational stability, this work opens up vast opportunities for titanium-oxo clusters in photocatalysis and provides a blueprint for developing sustainable cross-coupling methodologies.

Introduction

Aromatic amines are essential motifs in plenty of natural products, and pharmaceutical as well as agricultural chemicals,[1,2] rendering the development of efficient C–N bond formation methodologies a central focus in synthetic chemistry.[3] Since the pioneering work of Ullmann-type coupling documented by Ullmann and Goldberg, the transition-metal-catalyzed C–N cross-coupling has emerged as a research hotspot in the field of amination reactions.[4–6] Strategies such as copper-catalyzed C–N cross-coupling,[7] palladium-catalyzed C–N cross-coupling,[8] *etc.*, have been developed successively for constructing C–N bonds. Although remarkable advances have been made, the harsh conditions (*e.g.*, elevated temperature and strong alkoxide base environment) and their associated challenges, such as increased equipment costs and catalyst deactivation, still hinder the scale-up and broader applications of these synthetic methodologies.

Recently, light-driven dual-catalytic C–N cross-coupling utilizing nickel(II) catalysts coupled with photo-redox catalysts (PCs) has emerged as a new paradigm in amination.[9–11] These photo-mediated systems leverage earth-abundant nickel catalysts and photon energy to enable C–N cross-coupling under remarkably mild conditions, *i.e.*, substantially reduced reaction temperatures without base requirements, resulting in benefits in terms of cost and sustainability. In typical implementations, Ni salts such as $NiBr_2 \cdot 3H_2O$[10] and $NiCl_2 \cdot 6H_2O$[12] are usually utilized, following the formation of Ni(II)-amine complexes, which serve as acceptors for C–N cross-coupling systems. Meanwhile, the photo-induced energy/electron transfer (PET) could occur between PCs and the Ni–amine complexes, ultimately driving the C–N cross-coupling reactions. The PET process plays a vital role in the formation of C–N bonds in light-driven dual catalytic systems. However, the spatial isolation of nickel centers and photo-redox catalysts inherently restricts PET efficiency in separated dual catalytic systems, whether homogeneous or heterogeneous (Fig. 1a, left). Furthermore, the use of nickel salts in the reaction processes may lead to the formation of nickel black which causes catalyst deactivation. This necessitates the development of protective strategies to maintain catalytic activity.

In this context, we envision that developing an integrated dual catalysis system might yield a promising resolution (Fig. 1a, right). While several metal-oxo systems (*e.g.*, Zr^{4+}, W^{6+}, and Fe^{3+}) are capable of forming clusters and supporting structural functions,[13,14] Zr^{4+} clusters are usually too inert to be easily functionalized, and W^{6+} clusters may lack the necessary

---

[a] Collaborative Innovation Center of Advanced Nuclear Energy Technology, Institute of Nuclear and New Energy Technology, Tsinghua University, Beijing 100084, China. E-mail: yegang@mail.tsinghua.edu.cn

[b] School of Materials Science and Engineering, North Minzu University, Yinchuan 750021, China. E-mail: gaoq25@nmu.edu.cn

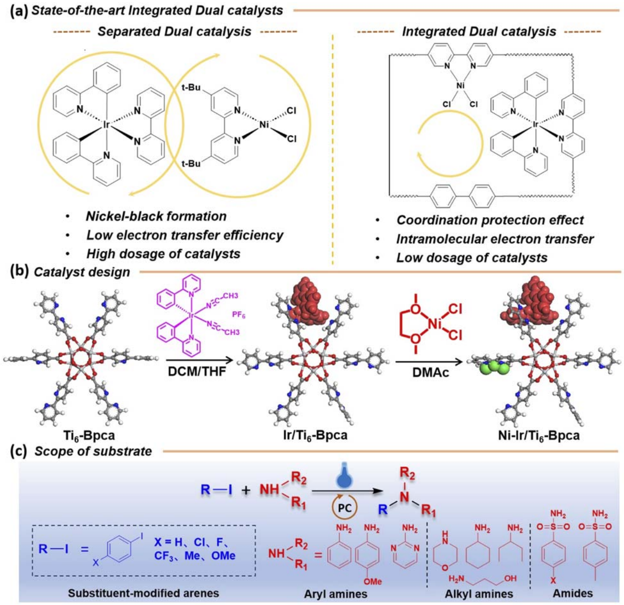

Fig. 1 (a) State-of-the-art integrated dual catalysis (left, separated dual catalysis; right, integrated dual catalysis). (b) Illustration of the Ti$_6$-cluster based dual catalyst design strategy; the red block is the [Ir(ppy)$_2$] complex in Ir/Ti$_6$-Bpca, and the green block is NiCl$_2$ in Ni–Ir/Ti$_6$-Bpca. (c) Available substrates for the established light-driven C–N cross-coupling strategy.

stability. Ti^{4+} achieves the best balance among Lewis acidity, thermal stability, and coordination activity, with unique advantages for constructing advanced heterometallic platforms. Ti-oxo clusters, particularly those based on the Ti$_6$O$_6$ core, exhibit superior and tunable optoelectronic properties, such as strong ligand-to-metal charge transfer (LMCT) characteristics in the visible region, and it can also undergo photochemical transformation by itself at ultraviolet wavelengths.[15,16] The integration of dual catalytic sites into engineered frameworks allows for the close arrangement of PCs and metal sites, enabling the PET process to proceed *via* an intramolecular pathway rather than an intermolecular one. Such integration may provide additional benefits of improving the reaction efficiency owing to the higher PET efficiency combined with metal centers positioned adjacent to transient radical species. Moreover, protective mechanisms could be achieved through rational design of the frameworks, leveraging their inherent connectivity and protective matrix. Titanium–oxygen clusters, as a member of the metal–oxygen cluster family, have attracted substantial attention owing to their diverse structural features and outstanding optical properties, enabling fantastic applications in photocatalysis,[17] energy storage,[18] as well as electrocatalysis.[19] Compared to porous frameworks, such as metal–organic frameworks (MOFs) or covalent-bond organic frameworks (COFs), clusters with isolated architectures exhibit higher catalytic activity owing to the higher diffusion dynamics. Notably, their isolated structures and tunable ligand components provide an ideal platform for accommodating catalytic sites.[20,21]

We present here a novel integrated dual catalysis system based on the surface engineering of titanium–oxygen clusters for efficient visible-light-driven C–N cross-coupling (Fig. 1b). A competitive coordination strategy was established to decorate titanium–oxygen clusters with bipyridine ligands bearing electron-rich nitrogen species.[22–24] The obtained Ti$_6$-Bpca clusters, having a molecular formula of [Ti$_6$O$_6$(O*i*Pr)$_6$(Bpca)$_6$] (where Bpca = 2,2'-bipyridine-5-carboxylic acid), serve as a favorable platform for synergistically anchoring Ni catalytic sites or Ir-based photo-sensitizers. With the nature of integrated structures, the dual catalyst incorporated titanium–oxygen clusters (Ni–Ir/Ti$_6$-Bpca) exhibited significantly enhanced photocatalytic activities compared to the separated dual catalytic counterparts (*i.e.*, the physical mixture of Ir photosensitizers and Ni salts). Particularly, the photo-induced electron transfer (PET) from Ir photosensitizers to Ni metal centers followed an intramolecular mechanism, which enhanced the PET efficiency and boosted the reaction activity. Moreover, the metal anchoring within the Ti$_6$-Bpca backbone prevented metal leaching and nickel-black formation, enabling a broad substrate scope encompassing amines (aryl, heteroaryl, and alkyl), carbamides, and sulfonamides with electron-rich, neutral, and poor (hetero)aryl iodides (Fig. 1c), maintaining high catalytic activity with an isolated yield up to 99%.

Results and discussion

The synthesis of Ti$_6$-Bpca clusters followed the procedure in the published work,[25] except that the ligand was changed from 4-aminobenzoic acid to 2,2′-bipyridine-5-carboxylic acid (Bpca). Besides, propionic acid was used as a competitive ligand to regulate the nucleation and growth kinetics of clusters, leading to the formation of the crystals. The synthesis details are described in the Experimental section of the SI. To examine the structures of the obtained Ti$_6$-Bpca clusters, characterization studies like Fourier transform infrared (FT-IR) spectroscopy, XRD analysis, and Pawley refinement were performed. The structural model was constructed and optimized with direct methods, force field calculations and Pawley refinement, combined with PXRD data. The results suggest that Ti$_6$-Bpca crystallizes in the triclinic crystal system (space group P_1) with the cell parameters $a = 15.687$ Å, $b = 15.295$ Å, $c = 17.161$ Å, $\alpha = 90.495°$, $\beta = 90.068°$, and $\gamma = 87.707°$ (residuals $R_{\mathrm{wp}} = 6.48\%$ and $R_{\mathrm{p}} = 5.06\%$) (Fig. 2a, Table S1, SI). Notably, the isolated Ti$_6$-Bpca clusters exhibit an ordered alignment driven by π–π stacking interactions between pyridine rings in adjacent clusters, as depicted in Fig. 2b. Each Ti$_6$-Bpca cluster features a Ti$_6$O$_6$ core adopting a hexagonal columnar geometry, stabilized equatorially by six bipyridine ligands. Along the vertical direction, the octahedral coordination sphere of each Ti^{4+} is completed by an isopropoxide anion. As shown in Fig. 2c, the FT-IR peaks at 1685 cm^{-1} of the free carboxylic group (C=O) disappeared after the synthesis of Ti–O clusters.[26] Notably, the medium peak at 420 cm^{-1} was ascribed to the Ti–O bond; both results indicated the coordination between Ti metal sites and carboxyl–O. The elemental analysis tests of C, H, and N and the C, N, O, and Ti contents obtained from XPS fitting show little

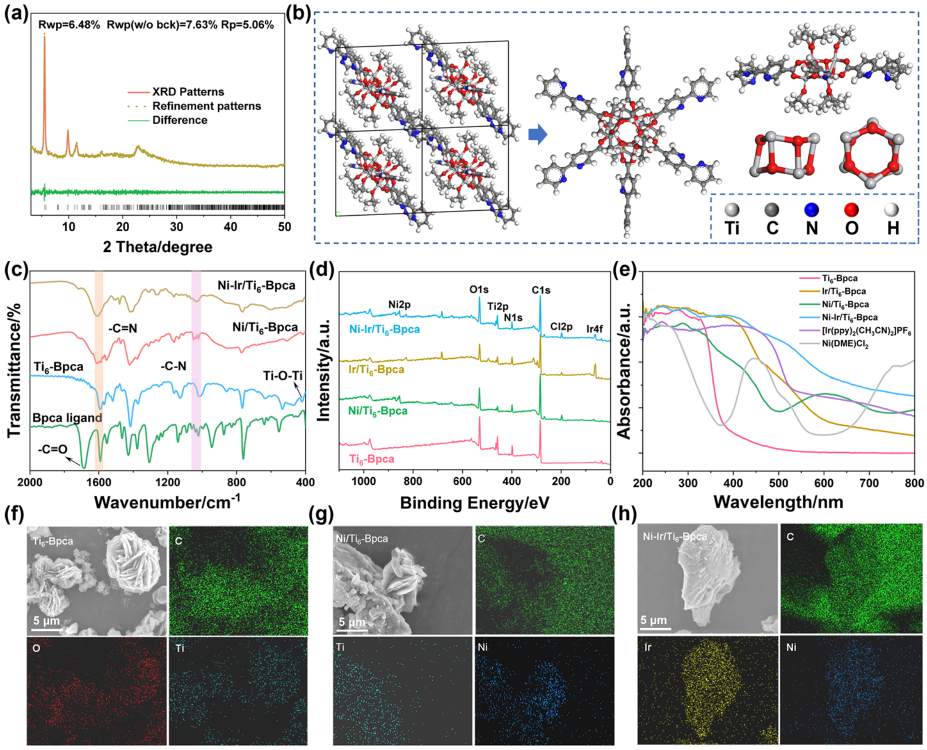

Fig. 2 (a) The XRD patterns and Pawley refinement of Ti_6-Bpca. (b) The detailed structures of Ti_6-Bpca (from left to right: the crystal structure, top of the Ti_6-Bpca cluster, side view of the Ti_6-Bpca cluster, and side view and top view of the Ti_6O_6 core). (c) The FT-IR spectra of Ti_6-Bpca, Ni/Ti_6-Bpca, Ir/Ti_6-Bpca, and Ni–Ir/Ti_6-Bpca. (d) The XPS survey of Ti_6-Bpca, Ni/Ti_6-Bpca, Ir/Ti_6-Bpca, and Ni–Ir/Ti_6-Bpca. (e) UV-vis-DRS spectra of Ti_6-Bpca, Ni/Ti_6-Bpca, Ir/Ti_6-Bpca, and Ni–Ir/Ti_6-Bpca. The SEM images of (f) Ti_6-Bpca, (g) Ni/Ti_6-Bpca and (h) Ni–Ir/Ti_6-Bpca.

difference from the theoretical elemental contents (Table S2), which also indicates the successful synthesis of the Ti_6-Bpca cluster and the accuracy of the proposed molecular formula.

The Ti_6-Bpca cluster bearing precisely positioned bipyridine units creates a versatile platform to accommodate catalytic metal sites. As a demonstration of the concept, a combination of iridium photosensitizers and nickel metal sites was incorporated into the Ti_6-Bpca clusters through a post-metallization strategy. First, the Ti_6-Bpca cluster was treated with $[Ir(ppy)_2(CH_3CN)_2]PF_6$ in a DCM/THF solvent mixture at 60 °C for Ir metalation at random sites of the clusters. Next, the obtained Ir/Ti_6-Bpca was further treated with $Ni(DME)Cl_2$ in the DMAc solvents at 60 °C, and the obtained active catalyst was named Ni–Ir/Ti_6-Bpca. After the metalation, the FT-IR peaks of the Bpca ligand at 1589 cm^{-1} and 1010 cm^{-1} are assigned to the –C=N and –C–N stretches, respectively. Upon coordination with Ir and Ni, these peaks shift to higher wavenumbers: to 1608 cm^{-1} and 1036 cm^{-1} after coordination with Ir, and to 1610 cm^{-1} and 1020 cm^{-1} after coordination with Ni (Fig. 2c and S1). The X-ray photoelectron spectroscopy (XPS) survey of Ni–Ir/Ti_6-Bpca included the characteristic peaks of Ir and Ni, confirming the successful incorporation of dual catalytic centers, as demonstrated in Fig. 2d. The XRD patterns for metallized samples exhibited broad peaks, indicating the nature of amorphous morphology, which could be attributed to the collapse of crystalline structures during the metalation procedure (Fig. S2). However, owing to the isolated characteristics of the clusters, the disruption of the periodicity does not impact their core structure. The UV-vis diffuse reflectance spectroscopy (DRS) analysis was conducted to study the physicochemical properties of Ti_6-Bpca and their metallized derivatives. The results suggested that after metallization, the Ti-oxo clusters exhibited broadband absorption in the wavelength range of 200–700 nm (Fig. 2e), indicating efficient visible-light absorption. Compared with the initial complexes $[Ir(ppy)_2(CH_3CN)_2]PF_6$ and $Ni(DME)Cl_2$, the metalated Ti-oxo clusters have corresponding enhancements in the visible light absorption intensity due to the new coordination environment formed with Ir and Ni. In particular, the Ti-oxo cluster coordinated with bimetallic Ni and Ir (Ni–Ir/Ti_6-Bpca) exhibits broader and stronger visible light absorption. The scanning electron microscopy (SEM) images further indicated that the overall morphology of Ti_6-Bpca clusters exhibited crystal characteristics, featuring a flower-like morphology, while those of metallized samples exhibited amorphous morphology (Fig. 2f–h). Besides, the energy-dispersive X-ray mapping images demonstrated that the metals were evenly distributed in the Ni–Ir/Ti_6-Bpca clusters (Fig. 2h), further confirming the successful creation of dual catalytic centers.

To verify the hypothesis we proposed in this work, the visible-light-mediated C–N cross-coupling reactions with metallized Ti-oxo clusters (Ni–Ir/Ti_6-Bpca) as catalysts were first evaluated. The coupling of iodobenzene **1** with aniline **2** was chosen as a model reaction and the optimized reaction conditions were investigated (Table 1). The photocatalytic C–N cross-coupling reaction was performed under blue LED (λ_{max} = 430 nm, 4 mW cm^{-2}) irradiation in acetonitrile solvent (CH_3CN, 1 mL) at room temperature (25 °C) in the presence of an organic base 1,2-dimethyl-1,4,5,6-tetrahydropyrimidine (DMTHPM, 0.8 mmol), resulting in an excellent catalytic performance with an isolated yield of around 93% of the coupled product **3** within 48 hours (Table 1, entry 1). Controlled experiments suggested that light illumination, photocatalysts, and an organic base were all required for the photocatalytic C–N cross-coupling reaction, while heating at 100 °C did not activate the reaction (Table 1, entries 2–5). For comparison, the catalytic systems utilizing Ir/Ti_6-Bpca, Ni/Ti_6-Bpca or Ti_6-Bpca as photocatalysts did not obtain target products (Table 1, entries 6–8). The effect of the organic base was investigated, and among all the organic bases used, DMTHPM exhibited the best catalytic performance (Table S3). Moreover, the effects of catalyst loading and base concentrations were also studied, and the results suggested that 1 mg catalysts and 0.2 mmol of DMTHPM base were the optimized conditions (Table S4). It is noteworthy that the physical mixtures of free metal precursors, *i.e.*, $[Ir(ppy)_2(CH_3CN)_2]PF_6$ and $Ni(DME)Cl_2$, gave a yield of only 3% under similar conditions (Table 1, entry 9), suggesting much more efficient electron transfer in the integrated dual catalytic system as compared to the separated system.

To gain insight into the high catalytic performance and mechanism of the integrated dual-catalytic system, the optical properties of the samples were first evaluated. The optical band gap energies E_g of the Ti-oxo clusters and their metallized derivatives were calculated *via* the Tauc plot method,[27] and the values were determined based on the intersection point of fitted lines in the linear region on the *X*-axis (Fig. 3a). The detailed information is displayed in Fig. S3–S6 (SI). According to the results of Tauc plot analysis, the band gap energies of Ti_6-Bpca decreased from 3.43 eV to below 3 eV after metalation, indicating the successful incorporation of Ir photosensitizers and Ni metal centers (Fig. 3b). To be specific, the E_g of these metallized samples was 2.52 eV, 2.54 eV, and 1.92 eV (for Ni/Ti_6-Bpca, Ir/Ti_6-Bpca, and Ni–Ir/Ti_6-Bpca), respectively. Ultraviolet photoelectron spectroscopy (UPS) measurements were conducted to investigate the detailed band structures of Ti-oxo clusters and their derivatives (Fig. 3c). The tangent lines were made to the linear part of the electron spectrum in both the low and high kinetic energy regions. The value of the intersection point on the *X*-axis was selected to calculate the positions of the valence band maximum energy E_{VBM}, and the conduction band minimum energy E_{CBM} was calculated with the difference between E_g and E_{VCM}. The detailed UPS spectra and calculation processes were discussed (Fig. S7–S10, SI). Combined with the results of the Tauc plot method and UPS spectral analysis, the band structures of Ti-oxo clusters and their derivatives were compared (Table S5). The results suggested that after metalation, E_{CBM} increased a lot. Specifically, the E_{CBM} of dual-metal installed sample Ni–Ir/Ti_6-Bpca increased from −4.13 eV to −2.36 eV. The lower E_g and the position of the CB suggested that Ni–Ir/Ti_6-Bpca was a good photosensitizer in the C–N cross-coupling system. Photoluminescence spectra revealed that upon excitation by visible light at 430 nm, Ni–Ir/Ti_6-Bpca exhibited emission at 588 nm (Fig. S11). From time-dependent emission studies, the excited-state average lifetime of Ni–Ir/Ti_6-Bpca was calculated to be 11.8 ns, whereas, for Ir and Ni precursor homogeneous mixtures, it was 8.4 ns (Fig. 3d). The

Table 1 Visible-light-mediated C–N cross-coupling reactions catalyzed by Ni–Ir/Ti_6-Bpca and the control experiments

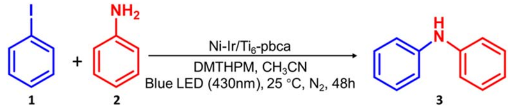

Entry	Reaction conditions	Yield (%)[b]
1	Optimized conditions[a]	93
2	Without light	0
3	Without base	0
4	Without a catalyst	0
5	Heating at 100 °C	0
6	Ir/Ti_6-Bpca	0
7	Ni/Ti_6-Bpca	0
8	Ti_6-Bpca	0
9	$[Ir(ppy)_2(CH_3CN)_2]PF_6$, $Ni(DME)Cl_2$[c]	3

[a] Optimized conditions: **1** (0.075 mmol), **2** (0.05 mmol), Ni–Ir/Ti_6-Bpca (1 mg), 1,2-dimethyl-1,4,5,6-tetrahydropyrimidine (DMTHPM, 0.2 mmol), and acetonitrile (CH_3CN, 1 mL) were added into a 5 mL sealed tube under protection of N_2; the reaction was carried under a blue light-emitting diode (LED) light with a wavelength of 430 nm (4 mW cm^{-2}) for 48 h. [b] Yield of **3** was determined by gas chromatography-mass spectrometry (GC-MS) using *p*-xylene as an internal standard. [c] 10 μL of DMAc was added as co-solvent of $Ni(DME)Cl_2$.

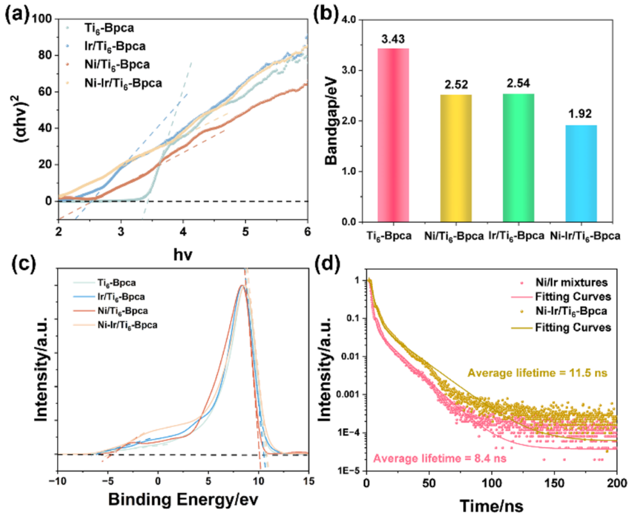

Fig. 3 (a) Tauc plot method calculated from UV-vis-DRS analysis and tangent line from fitting of the linear region to calculate bandgap energy (E_g) of Ti_6-Bpca and metallized Ti_6-Bpca. (b) The summary bar graph of bandgap energies calculated from Tauc plot method for Ti_6-Bpca and metallized Ti_6-Bpca. (c) Overall UPS spectra and tangent line fitting in the range of low and high binding energy regions for calculation of E_L and E_H for Ti_6-Bpca and metallized Ti_6-Bpca. (d) Fluorescence lifetime tests of Ti_6-Bpca and metallized Ti_6-Bpca.

results of lifetime measurement confirmed the efficient electron transfer in the integrated dual-catalytic system compared to the separated dual-catalytic system, thus resulting in promoted catalytic efficiency.

The underlying mechanisms responsible for dual-catalytic C–N cross-coupling reactions have been extensively discussed recently,[28,29] especially for Ir/Ni dual-catalytic systems.[30–33] Considering the nature of the integrated dual-catalytic system, a base-assisted electron transfer process might occur in the dual-catalytic cross-coupling reactions. To verify this hypothesis, steady-state emission quenching was employed to examine the charge transfer between excited metallized clusters and substrates. The quenching efficiency was quantified with the Stern–Volmer equation $(I_0/I) = 1 + K_{SV}[Q]$. Consequently, the addition of a mixture of organic base (DMTHPM) with aniline led to substantial fluorescence quenching with a high quenching constant ($K_{SV} = 2.666$ mM^{-1}) (Fig. S12), confirming the critical role of base (Fig. 4a, left).

To study the potential electron transfer mechanism from the photo-sensitive centers (Ir) to the catalytic centers (Ni) inside the integrated system while optimizing their distribution, DFT calculations for molecular orbital properties of photo-redox catalysts were performed using Gaussian 16 software.[34] First, the possible location of Ir and Ni centers was determined (Fig. 4a, right). To balance the computational efficiency and accuracy, we streamlined the models by eliminating the isopropoxide anion binding on the Ti_6O_6 cores in the vertical direction. It is noteworthy that, as revealed in the results of simultaneous inductively coupled plasma atomic emission spectroscopy (ICP-OES, Table S6), the Ir and Ni loadings in each cluster with respect to the bipyridine (Bpy) ligand are 31.36% w.r.t. the Bpy unit (Ir) and 20.27% w.r.t. the Bpy unit (Ni), respectively. For clarity, we only consider the case where each cluster is loaded with one Ir center and one Ni center, and the ratio of Ir and Ni was set as 1 : 1 in the following calculations. If the Ir center was pre-located, there existed three potential positions of Ni centers, adjacent, alternate, and opposite positions, which were termed Ni–Ir/Ti_6-Bpca_*x* ($x = 1, 2, 3$), respectively. Geometries were optimized using Gaussian packages at the B3LYP/6-311G (d, p) theory level;[35] electrostatic potential (ESP) analysis, and molecular orbital property calculations were performed at the same level using a continuum solvation model (SMD) with acetonitrile as the solvent.[36]

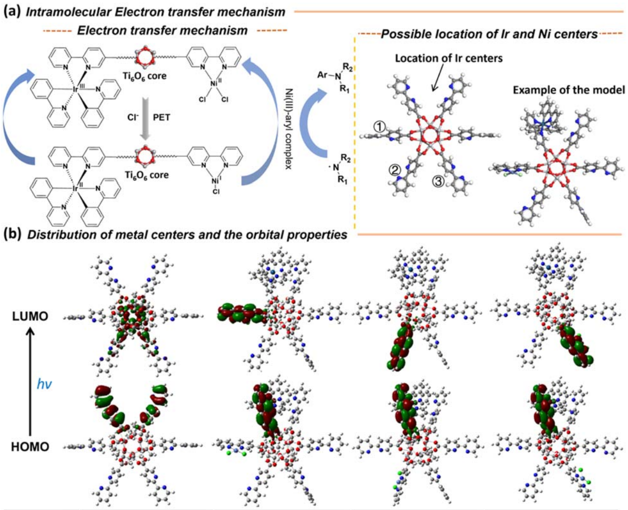

Molecules	Ti_6-Bpca			Ni-Ir/Ti_6-Bpca_1			Ni-Ir/Ti_6-Bpca_2			Ni-Ir/Ti_6-Bpca_3		
Molecular orbitals	HOMO (eV)	LUMO (eV)	ΔE (eV)	HOMO (eV)	LUMO (eV)	ΔE (eV)	HOMO (eV)	LUMO (eV)	ΔE (eV)	HOMO (eV)	LUMO (eV)	ΔE (eV)
	-6.77	-2.47	4.30	-4.43	-2.22	2.20	-4.39	-2.29	2.10	-4.25	-2.19	2.06

Fig. 4 (a) Illustration of the intramolecular electron transfer mechanism (electron transfer mechanism, left; possible location of Ir and Ni centers, right). (b) Optimized distribution of Ir and Ni centers; table below: the calculated molecular orbitals of Ti_6-Bpca, Ni–Ir/Ti_6-Bpca_1, Ni–Ir/Ti_6-Bpca_2, and Ni–Ir/Ti_6-Bpca_3.

First, the molecular orbital properties of Ti_6-Bpca were evaluated, as displayed in Fig. 4b. Obviously, the HOMOs were mainly located on the bipyridine ligands, while the LUMOs were mainly contributed by the Ti_6O_6 cores. As for metallized Ti-oxo clusters, the HOMOs were primarily distributed on the Ir centers, whereas the LUMOs were ascribed to the Ni centers. This implies that, upon exposure to light, the Ir centers could serve as photon antennas to absorb light with a suitable wavelength and transfer excited electrons to Ni centers, thus triggering C–N cross-coupling reactions. To optimize the positions of Ir and Ni centers, the calculated energy gaps (ΔE) of the HOMO and LUMO of the above-mentioned models have also been studied. In comparison, all the calculated energy gaps (ΔE) were overestimated as compared to the experiment values, which was likely due to the incorporation of hybrid density functional exchange in B3LYP.[37,38] It was noteworthy that, after the incorporation of bimetallic centers, the values of ΔE significantly reduced (for Ti_6-Bpca and Ni–Ir/Ti_6-Bpca_1–3, it was 4.30, 2.20, 2.10, and 2.06 eV, respectively), which was mainly attributed to the delocalized nature of Ir photosensitizers. As discussed above, it was concluded that all three models exhibited comparable bandgap energies, confirming the efficient intramolecular electron transfer in the dual-catalytic systems. Based on our experimental results and precedent literature on dual photoredox/nickel catalysis,[39,40] we propose a more detailed catalytic cycle for the Ir/Ni-mediated C–N cross-coupling (Fig. 4a). Initially, photoexcitation of the Ir(III) photosensitizer followed by reductive quenching generates the strongly reducing Ir(II) species. Crucially, clustered intramolecular electron transfer from Ir(II) to the Ni(II) center within the assembled system generates a key Ni(I) intermediate. This critical step unlocks the catalytic potency of nickel. The proposed cycle then proceeds through a Ni(I)/Ni(III) manifold. The nucleophilic Ni(I) species undergoes oxidative addition with the aryl electrophile (*e.g.*, aryl iodine), yielding a Ni(III)-aryl complex. Subsequent transmetalation with the deprotonated amine substrate forms a Ni(III)-amido complex. Finally, reductive elimination affords the desired C–N coupled product and regenerates the Ni(II) catalyst, closing the catalytic cycle. This mechanism highlights the dual role of our molecular catalyst: the Ir center acts as a photosensitizer to harness light energy and deliver electrons, while the Ni center orchestrates the key bond-forming steps through its dynamic oxidation states (Ni(II) → Ni(I) → Ni(III) → Ni(II)).

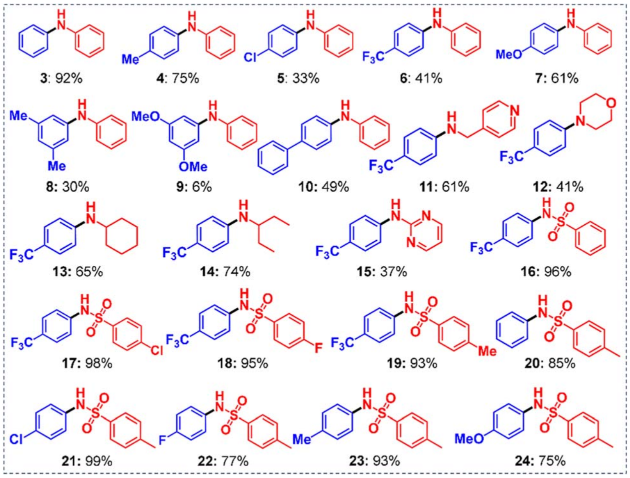

Fig. 5 Scope of reaction substrates utilized in this article.

Finally, we tested the catalytic performance of C–N coupling at different time points to evaluate the reaction kinetics of the catalytic system. The data show a rapid reaction within the first 24 hours (80% yield), followed by a slower gradual increase to 93% yield at 48 hours (Fig. S13). We also systematically evaluated the versatility and efficiency of the dual-metalated Ti-oxo clusters as a visible-light-driven photocatalyst for C–N cross-coupling reactions (Fig. 5). In order to compare the catalytic efficiency, we conducted all reactions under the same conditions. The cross-coupling reactions with a series of functional group (methyl, chlorine, trifluoromethyl, methoxy, and phenylmethyl) substituted aryl iodides proceeded well to generate products **3–10** with yields in the range of 6–93%. Notably, all the C–N coupled products were isolated with high chemo-selectivity. The investigation then focused on the scope of the arylamine coupling partners. 4-Iodotrifluoromethylbenzene was selected as the halide coupling partner due to its significant applications in pharmaceuticals and agrochemicals.[41] Significantly, the light-driven C–N cross-coupling reactions also proceeded smoothly with pyridin-4-ylmethanamine (**11**), morpholine (**12**), cyclohexylamine (**13**), pentan-3-amine (**14**), and pyrimidyl amine (**15**) with good to excellent yields of 37–74%. Moreover, the Ni–Ir/Ti_6-Bpca-catalyzed light-driven C–N cross-coupling reaction could be further extended to the sulfonamide coupling partners. Excellent yields (>75%) of *N*-aryl sulfonamides (**16–19**) were obtained with diversely substituted sulfonamides. Different electronically biased substituents at the *p*-position of the aryl iodide coupling partner reacted smoothly, delivering the yields of products in 75–99%. In addition, the metal leaching of Ni–Ir/Ti_6-Bpca catalysts was examined. The Ni–Ir/Ti_6-Bpca catalyst was filtered after coupling of **1** and **2**, and the reaction solvents were tested *via* ICP-OES. A negligible leaching ratio of Ni metal centers around 1% was observed (Table S7), indicating the protection effect of bipyridine ligands.

Conclusions

In summary, we have developed in this study a novel integrated dual-catalytic system with dual-metallized Ti-oxo clusters as photo-redox catalysts towards the light-driven C–N cross-coupling reaction. The strategically incorporated bipyridine ligands provide multiple electron-rich nitrogen sites for precise metal coordination, creating synergistic catalytic centers that facilitate the photochemical coupling process. The structures and optical properties of the metallized Ti-oxo clusters were carefully studied and DFT calculations were employed to investigate the PET-involved reaction mechanism. This study demonstrated that, through synergistic incorporation of Ir and Ni centers into surface-engineered Ti-oxo clusters, the electron transfer efficiency was boosted as compared to that of the separated dual-catalytic system, through an intramolecular electron transfer mechanism. Therefore, the resulting catalyst Ni–Ir/Ti_6-Bpca exhibited high catalytic activity with a broad substrate scope and excellent functional group tolerance. Additional advantages of this integrated heterogeneous photocatalytic system lie in the inhibition of metal site leaching and nickel black formation through the coordination protection effect, as well as the lower dosage of catalysts due to the significant electron transfer efficiency. This advancement is poised to significantly accelerate the development of industrial-friendly C–N cross-coupling synthesis strategies. Beyond these implications, this study broadens the potential applications of Ti-oxo clusters in heterogeneous catalysis while providing fresh perspectives and innovative methodological frameworks for photocatalytic research.

Author contributions

G. Y. designed the study and supervised the project. Q. G. performed the DFT calculations. S. W., J. J., and Y. W. performed the experiments. All the authors discussed the results and co-wrote the manuscript.

Conflicts of interest

There are no conflicts to declare.

Data availability

All experimental data and procedures are available in the SI. Supplementary information: additional characterization data (including XRD patterns, FT-IR spectra, and GC-MS results, *etc.*), detailed experimental procedures for catalyst synthesis, and results of control experiments discussed in the main text. See DOI: **https://doi.org/10.1039/d5sc04675k**.

Acknowledgements

We acknowledge the Nuclear Technology R&D Program and the National Natural Science Foundation of China (No. 22376117) for the financial support of this work.

Notes and references

1 J. Bariwal and E. Van der Eycken, C–N Bond Forming Cross-Coupling Reactions: An Overview, *Chem. Soc. Rev.*, 2013, **42**, 9283–9303.

2 A. Y. Chan, I. B. Perry, N. B. Bissonnette, B. F. Buksh, G. A. Edwards, L. I. Frye, O. L. Garry, M. N. Lavagnino, B. X. Li, Y. Liang, E. Mao, A. Millet, J. V. Oakley, N. L. Reed, H. A. Sakai, C. P. Seath and D. W. C. MacMillan, Metallaphotoredox: The Merger of Photoredox and Transition Metal Catalysis, *Chem. Rev.*, 2022, **122**, 1485–1542.

3 N. E. S. Tay, D. Lehnherr and T. Rovis, Photons or Electrons? A Critical Comparison of Electrochemistry and Photoredox Catalysis for Organic Synthesis, *Chem. Rev.*, 2022, **122**, 2487–2649.

4 I. Goldberg, Ueber Phenylirungen Bei Gegenwart Von Kupfer Als Katalysator, *Ber. Dtsch. Chem. Ges.*, 1906, **39**, 1691–1692.

5 F. Ullmann, Ueber Eine Neue Bildungsweise Von Diphenylaminderivaten, *Ber. Dtsch. Chem. Ges.*, 1903, **36**, 2382–2384.

6 L. Peng, Z. Hu, Z. Tang, Y. Jiao and X. Xu, Recent Progress in Transition Metal Catalyzed Cross Coupling of Nitroarenes, *Chin. Chem. Lett.*, 2019, **30**, 1481–1487.

7 I. P. Beletskaya and A. V. Cheprakov, Copper in Cross-Coupling Reactions-the Post-Ullmann Chemistry, *Coord. Chem. Rev.*, 2004, **248**, 2337–2364.

8 P. Ruiz-Castillo and S. L. Buchwald, Applications of Palladium-Catalyzed C-N Cross-Coupling Reactions, *Chem. Rev.*, 2016, **116**, 12564–12649.

9 M. S. Oderinde, N. H. Jones, A. Juneau, M. Frenette, B. Aquila, S. Tentarelli, D. W. Robbins and J. W. Johannes, Highly Chemoselective Iridium Photoredox and Nickel Catalysis for the Cross-Coupling of Primary Aryl Amines with Aryl Halides, *Angew. Chem., Int. Ed.*, 2016, **55**, 13219–13223.

10 C.-H. Lim, M. Kudisch, B. Liu and G. M. Miyake, C-N Cross-Coupling Via Photoexcitation of Nickel-Amine Complexes, *J. Am. Chem. Soc.*, 2018, **140**, 7667–7673.

11 E. B. Corcoran, M. T. Pirnot, S. Lin, S. D. Dreher, D. A. DiRocco, I. W. Davies, S. L. Buchwald and D. W. C. MacMillan, Aryl Amination Using Ligand-Free Ni(II) Salts and Photoredox Catalysis, *Science*, 2016, **353**, 279–283.

12 Y.-Y. Liu, D. Liang, L.-Q. Lu and W.-J. Xiao, Practical Heterogeneous Photoredox/Nickel Dual Catalysis for C-N and C-O Coupling Reactions, *Chem. Commun.*, 2019, **55**, 4853–4856.

13 K. Declerck, N. D. Savić, M. J. Parammal, C. Seno, G. Bruylants, J. De Roo and T. N. Parac-Vogt, Harnessing the Dynamic Nature of a Zirconium-Oxo Nanocluster for Reversible Protein Capture and Proteolysis, *Angew. Chem., Int. Ed.*, 2025, e202512482.

14 S.-S. Wang and G.-Y. Yang, Recent Advances in Polyoxometalate-Catalyzed Reactions, *Chem. Rev.*, 2015, **115**, 4893–4962.

15 S. E. Brown, I. Mantaloufa, R. T. Andrews, T. J. Barnes, M. R. Lees, F. De Proft, A. V. Cunha and S. D. Pike, Photoactivation of Titanium-Oxo Cluster $[Ti_6O_6(OR)_6(O_2C^tBu)_6]$: Mechanism, Photoactivated Structures, and Onward Reactivity with O_2 to a Peroxide Complex, *Chem. Sci.*, 2023, **14**, 675–683.

16 S. E. Brown, M. R. Warren, D. J. Kubicki, A. Fitzpatrick and S. D. Pike, Photoinitiated Single-Crystal to Single-Crystal Redox Transformations of Titanium-Oxo Clusters, *J. Am. Chem. Soc.*, 2024, **146**, 17325–17333.

17 E.-M. Han, W.-D. Yu, J. Yan, X.-Y. Yi and C. Liu, Metal-Directed Self-Assembly of $\{Ti_8l_2\}$ Cluster-Based Coordination Polymers with Enhanced Photocatalytic Alcohol Oxidation Activity, *Inorg. Chem.*, 2022, **61**, 923–930.

18 X. Bai, G. Zhao, G. Yang, M. Wang, Z. Chen and N. Zhang, Titanium-Oxygen Clusters Brazing Li with $Li_{6.5}La_3Zr_{1.5}Ta_{0.5}O_{12}$ for High-Performance All-Solid-State Li Batteries, *Nano Lett.*, 2023, **23**, 7934–7940.

19 Y.-Q. Tian, E.-M. Han, B. Wan, W.-D. Yu, M.-Z. Chen, J. Yan, X.-Y. Yi and C. Liu, Heterometallic Polyoxotitanium Clusters as Bifunctional Electrocatalysts for Overall Water Splitting, *Inorg. Chem.*, 2022, **61**, 10151–10158.

20 H. Shi, J. Du, H. Wang, Z. Jia, D. Jin, J. Cao, J. Hou and X. Guo, Engineering Unsaturated Coordination of Conductive TiOx Clusters Derived from Metal-Organic-Framework Incorporated into Hollow Semiconductor for Highly Selective CO_2 Photoreduction, *Chem. Eng. J.*, 2022, **440**, 135735.

21 L.-R. Liao, D.-C. Zheng, P.-X. Ou, Q.-X. Zhao, W.-M. Xuan and Q. Zheng, π-Conjugated Chromophore Functionalized High-Nuclearity Titanium-Oxo Clusters Containing Structural Unit of Anatase for Photocatalytic Selective Oxidation of Sulfides, *Rare Met.*, 2024, **43**, 1736–1746.

22 Y.-Y. Zhu, G. Lan, Y. Fan, S. S. Veroneau, Y. Song, D. Micheroni and W. Lin, Merging Photoredox and Organometallic Catalysts in a Metal-Organic Framework Significantly Boosts Photocatalytic Activities, *Angew. Chem., Int. Ed.*, 2018, **57**, 14090–14094.

23 A. Jati, K. Dey, M. Nurhuda, M. A. Addicoat, R. Banerjee and B. Maji, Dual Metalation in a Two-Dimensional Covalent Organic Framework for Photocatalytic C-N Cross-Coupling Reactions, *J. Am. Chem. Soc.*, 2022, **144**, 7822–7833.

24 G. Lan, Z. Li, S. S. Veroneau, Y.-Y. Zhu, Z. Xu, C. Wang and W. Lin, Photosensitizing Metal-Organic Layers for Efficient Sunlight-Driven Carbon Dioxide Reduction, *J. Am. Chem. Soc.*, 2018, **140**, 12369–12373.

25 K. Hong and H. Chun, Nonporous Titanium-Oxo Molecular Clusters That Reversibly and Selectively Adsorb Carbon Dioxide, *Inorg. Chem.*, 2013, **52**, 9705–9707.

26 B. P. Singh, V. Choudhary, S. Teotia, D. T. Gupta, V. N. Singh, S. Dhakate and R. B. Mathur, Solvent Free, Efficient, Industrially Viable, Fast Dispersion Process Based Amine Modified MWCNT Reinforced Epoxy Composites of Superior Mechanical Properties, *Adv. Mater. Lett.*, 2015, **6**, 104–113.

27 J. Tauc, R. Grigorov and A. Vancu, Optical Properties and Electronic Structure of Amorphous Germanium, *J. Phys. Soc. Jpn.*, 1966, **21**, 123.

28 X. Qi, Y. Li, R. Bai and Y. Lan, Mechanism of Rhodium-Catalyzed C-H Functionalization: Advances in Theoretical Investigation, *Acc. Chem. Res.*, 2017, **50**, 2799–2808.

29 M.-Y. Qi, M. Conte, M. Anpo, Z.-R. Tang and Y.-J. Xu, Cooperative Coupling of Oxidative Organic Synthesis and Hydrogen Production over Semiconductor-Based Photocatalysts, *Chem. Rev.*, 2021, **121**, 13051–13085.

30 Z. Li, Y. Li, H. Cheng, Y. Song, Y. Jiao, S. Shi, J. Gao, L. Sun and J. Hou, Atomically Dispersed Ni Active Sites on Covalent Organic Frameworks for Heterogeneous Metallaphotocatalytic C-N Cross-Coupling, *Appl. Catal., B*, 2024, **345**, 123698.

31 Y.-L. Li, F. Wang, J. J. Vittal, P. Jin, S.-L. Huang and G.-Y. Yang, Incorporation of $Ir(C^\wedge N)_2(N^\wedge N)$-$NiCl_2$ in a (N^N)-Covalent Organic Framework for Transcendent Dual Catalysis in Photochemical Cross-Coupling Synthesis, *J. Mater. Chem. A*, 2024, **12**, 9164–9172.

32 C. H. Basch, J. Liao, J. Xu, J. J. Piane and M. P. Watson, Harnessing Alkyl Amines as Electrophiles for Nickel-Catalyzed Cross Couplings Via C-N Bond Activation, *J. Am. Chem. Soc.*, 2017, **139**, 5313–5316.

33 L.-Y. Bao, R.-W. Gao, S. Wang, R.-H. Li, B. Zhu, Z.-M. Su and W. Guan, Theoretical Study of Ni^{I}-Ni^{III} Cycle Mediated by Heterogeneous Zinc in C-N Cross-Coupling Reaction, *Phys. Chem. Chem. Phys.*, 2022, **24**, 7617–7623.

34 M. J. Frisch, G. W. Trucks, H. B. Schlegel, G. E. Scuseria, M. A. Robb, J. R. Cheeseman, G. Scalmani, V. Barone, G. A. Petersson, H. Nakatsuji, X. Li, M. Caricato, A. V. Marenich, J. Bloino, B. G. Janesko, R. Gomperts, B. Mennucci, H. P. Hratchian, J. V. Ortiz, A. F. Izmaylov, J. L. Sonnenberg, D. Williams-Young, F. Ding, F. Lipparini, F. Egidi, J. Goings, B. Peng, A. Petrone, T. Henderson, D. Ranasinghe, V. G. Zakrzewski, J. Gao, N. Rega, G. Zheng, W. Liang, M. Hada, M. Ehara, K. Toyota, R. Fukuda, J. Hasegawa, M. Ishida, T. Nakajima, Y. Honda, O. Kitao, H. Nakai, T. Vreven, K. Throssell, J. A. Montgomery Jr., J. E. Peralta, F. Ogliaro, M. J. Bearpark, J. J. Heyd, E. N. Brothers, K. N. Kudin, V. N. Staroverov, T. A. Keith, R. Kobayashi, J. Normand, K. Raghavachari, A. P. Rendell, J. C. Burant, S. S. Iyengar, J. Tomasi, M. Cossi, J. M. Millam, M. Klene, C. Adamo, R. Cammi, J. W. Ochterski, R. L. Martin, K. Morokuma, O. Farkas, J. B. Foresman, and D. J. Fox, *Gaussian 16*, Gaussian Inc., Wallingford CT, 2016.

35 A. D. Becke, Density-Functional Thermochemistry. III. The Role of Exact Exchange, *J. Chem. Phys.*, 1993, **98**, 5648–5652.

36 J. Leech, J. F. Prins and J. Hermans, SMD: Visual Steering of Molecular Dynamics for Protein Design, *IEEE Comput. Sci. Eng.*, 1996, **3**, 38–45.

37 M. Wykes, B. Milian-Medina and J. Gierschner, Computational Engineering of Low Bandgap Copolymers, *Front. Chem.*, 2013, **1**, 00035.

38 Z. Rostami, A. Hosseinian and A. Monfared, DFT Results against Experimental Data for Electronic Properties of C60 and C70 Fullerene Derivatives, *J. Mol. Graphics Modell.*, 2018, **81**, 60–67.

39 H. Ren, G.-F. Li, B. Zhu, X.-D. Lv, L.-S. Yao, X.-L. Wang, Z.-M. Su and W. Guan, How Does Iridium(III) Photocatalyst Regulate Nickel(II) Catalyst in Metallaphotoredox-Catalyzed C–S Cross-Coupling? Theoretical and Experimental Insights, *ACS Catal.*, 2019, **9**, 3858–3865.

40 R.-H. Li, B. Zhu, S. Wang, Y. Geng, L.-K. Yan, Z.-M. Su, L.-S. Yao, R.-L. Zhong and W. Guan, Theoretical Mechanistic Study of Metallaphotoredox Catalysis: C–N Cross-Coupling Via Ni(II)-Mediated σ-Bond Metathesis, *Org. Chem. Front.*, 2020, **7**, 2168–2178.

41 M. Tsukamoto, T. Nakamura, H. Kimura and H. Nakayama, Synthesis and Application of Trifluoromethylpyridines as a Key Structural Motif in Active Agrochemical and Pharmaceutical Ingredients, *J. Pestic. Sci.*, 2021, **46**, 125–142.